Available online at www.sciencedirect.com
ScienceDirect
International Journal of Mass Spectrometry 265 (2007) 388–400
International Journal of Mass Spectrometry
www.elsevier.com/locate/ijms

Probing the potential energy landscape for dissociation of protonated indole via threshold collision-induced dissociation and theoretical studies

Zhibo Yang, Chunhai Ruan, H. Ahmed, M.T. Rodgers *

Department of Chemistry, Wayne State University, Detroit, MI 48202, USA

Received 20 November 2006; received in revised form 21 June 2007; accepted 21 June 2007
Available online 28 June 2007

In honor of J.H. Futrell in thanks for his numerous contributions to gas-phase ion chemistry and mass spectrometry, and in appreciation of his friendship.

Abstract

Collision-induced dissociation of protonated indole with Xe is studied as a function of kinetic energy using guided ion beam tandem mass spectrometry techniques. Activated dissociation resulting in endothermic loss of neutral HCN (or HNC) is the only pathway observed over the range of collision energies examined. The cross-section threshold for this activated dissociation pathway is interpreted to yield 0 and 298 K activation energies for this process after accounting for the effects of multiple ion–neutral collisions, the internal energy distribution of the protonated indole cations, and their lifetimes for dissociation. Density functional theory (DFT) calculations at the MPW1PW91/6-31G* level of theory are used to determine the structures of indole, the protonated indole tautomers, and the transition states, intermediates, and products involved in the activated dissociation of protonated indole. Four distinct pathways between the reactant ion and dissociation products are computed. In all cases, the ionic product formed is $C_6H_5CH_2^+$, while the neutral product is HCN in three of the pathways and HNC in the fourth. The vibrational frequencies and rotational constants of the ground state tautomer of protonated indole and the rate-determining transition state along each of the pathways computed are used for the thermodynamic analysis of the experimental data. The theoretical activation energies and potential energy landscapes for activated dissociation of protonated indole are determined from single point calculations at the MPW1PW91/6-311+G(2d,2p) and MP2(full)/6-311+G(2d,2p) levels of theory, using the MPW1PW91/6-31G* optimized geometries. Both theories produce similar potential energy landscapes for elimination of HCN (or HNC) from protonated indole. Theory suggests that elimination of HNC is favored over HCN. However, our threshold measurements probe the lowest-energy pathway available and are in much better agreement with the higher-energy HCN elimination pathways, suggesting that theory underestimates the activation energy for loss of HNC.

Keywords: Activation energy; Guided ion beam; Indole; Proton affinity; Threshold collision-induced dissociation

1. Introduction

Indole is a building block of many natural products, functions as an essential constituent of perfumes [1], and has been shown to suppress the hepatotoxicity and carcinogenicity of several carcinogens [2]. Many derivatives of indole have important properties and have been widely used as aroma compound precursors [3,4], plant growth regulators [5], inhibitors of blood coagulation [6], and as promising compounds for fungicide [7], anti-tumor [8,9], and anti-HIV [10] medicines. As the side chain of tryptophan (Trp), indole is involved in a variety of biological processes and has been studied as a model system in spectroscopic studies to extract structures and dynamical properties of proteins [11–13] as well as to investigate cation–π interactions between tryptophan and metal cations [14,15]. Therefore, the properties, reactions, and mass spectrum of indole and its derivatives are of interest in both fundamental and pharmaceutical studies.

Much of our recent work has made use of quantitative threshold collision-induced dissociation (TCID) methods to obtain accurate thermodynamic information on a variety of noncovalently bound metal–ligand complexes. These studies have either directly probed the interaction between metal ions and organic [16–28] and biological ligands [29–36], or have examined solvation of metal ions by various solvents [37–41]. The simple noncovalent bond cleavages observed in these systems have allowed accurate bond dissociation energies (BDEs) to be

* Corresponding author.
E-mail address: mrodgers@chem.wayne.edu (M.T. Rodgers).

1387-3806/$ – see front matter © 2007 Elsevier B.V. All rights reserved.
doi:10.1016/j.ijms.2007.06.016

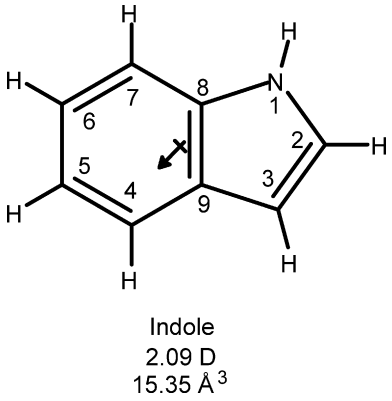

Fig. 1. Structure of indole. The properly scaled and oriented dipole moment in Debye (calculated here) is shown as an arrow. The estimated polarizability is also shown [15].

determined using a loose phase space limit (PSL) transition state (TS) model [42]. In the present study, we use guided ion beam mass spectrometry to collisionally excite protonated indole leading to isomerization and covalent bond cleavage and resulting in elimination of neutral HCN (or HNC). The structure of indole is shown in Fig. 1 along with its calculated dipole moment and estimated polarizability [15]. The kinetic energy-dependent cross-section for the observed CID process is analyzed using methods developed previously [42–44]. The analysis explicitly includes the effects of the internal and translational energy distributions of the reactants, multiple ion–neutral collisions, and the lifetimes for dissociation. In contrast to the *absolute BDEs* measured in our earlier work, the threshold energies derived in the present study provide the *activation energy* for loss of HCN (or HNC) from protonated indole. The measured activation energy is compared to theoretical estimates for the rate-limiting transition state along four distinct potential energy surfaces computed for the observed dissociation pathway.

2. Experimental

2.1. General procedures

The cross-section for collision-induced dissociation (CID) of protonated indole is measured using a guided ion beam tandem mass spectrometer that has been described in detail previously [19]. However, in the current study a new microwave discharge source is employed for ion generation. A schematic representation of the instrument including the microwave discharge source is shown in Fig. 2, while a detailed picture of the microwave discharge source is shown in Fig. 3. The microwave discharge source is simple in design. The ion source volume is simply a 0.5″ o.d. × 4″ long quartz tube through which the He carrier gas passes. The quartz tube is surrounded by an Evenson microwave cavity operated continuously at 2.45 GHz and powered by an Opthos Instruments MPG-4 CW microwave generator, typically at 20–30 W forward power (reflected power is typically <10%). The Evenson cavity has two adjustments that can be made to optimize the power-transfer process. It also has an air-cooling port to allow cooling of the source. The microwave discharge source is coupled to our flow tube, and is mounted at an angle of

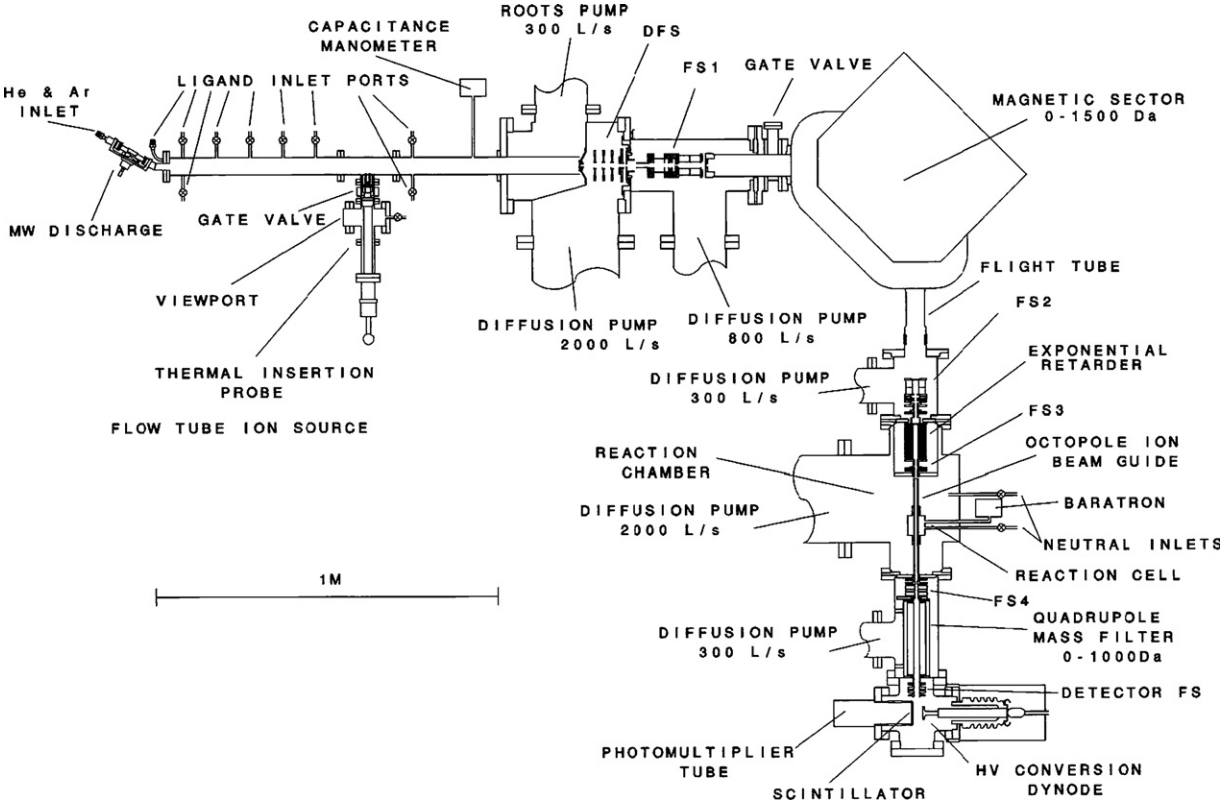

Fig. 2. Schematic diagram of the guided ion beam tandem mass spectrometer.

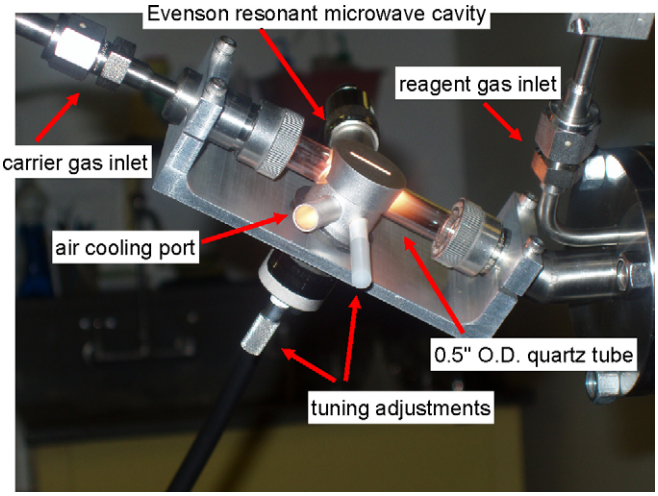

Fig. 3. Detailed picture of the microwave discharge source.

45° relative to the flow tube to minimize passage of UV ionizing radiation from the source region into the flow tube. Indole vapor is introduced into the flow tube ∼5 cm downstream from the microwave cavity. Indole radical cations are formed by collisions of indole vapor with metastable He atoms and ions generated in the microwave discharge. Protonated indole is then formed by proton-transfer reactions between the indole radical cations and neutral indole. The ions undergo $>10^5$ collisions with the He bath gas (∼0.7 Torr), such that the internal energies of the ions emanating from the source are assumed to be well described by a Maxwell–Boltzmann distribution at room temperature [19].

The ions are effusively sampled from the source, focused, accelerated, and focused into a magnetic sector momentum analyzer for reactant mass analysis. Mass-selected ions are decelerated to a desired kinetic energy and focused into an octopole ion beam guide. The octopole passes through a static gas cell containing Xe at low pressure (0.05–0.20 mTorr), to ensure that multiple ion–neutral collisions are unlikely. The octopole ion guide acts as an efficient radial ion trap. Therefore, loss of scattered reactant and product ions in the octopole region is almost entirely eliminated [45,46]. Ions drift to the end of the octopole where they are focused into a quadrupole mass filter for mass analysis, and subsequently detected with a secondary electron scintillation detector and standard pulse counting techniques.

Product ion intensities are converted to absolute cross-sections using a Beer's law analysis [47]. Errors in the pressure measurement and the length of the interaction region typically result in absolute uncertainties of ±20% in the cross-section magnitudes. Relative uncertainties are approximately ±5%.

Ion kinetic energies in the laboratory frame, E_{lab}, are converted to energies in the center-of-mass (CM) frame, E_{CM} using the formula $E_{CM} = E_{lab}m/(m+M)$, where M and m are the masses of the ionic ($C_8H_7N^+$) and neutral (Xe) reactants, respectively. All energies reported below are in the CM frame unless otherwise noted. The absolute zero and distribution of the ion kinetic energies are determined using the octopole ion guide as a retarding potential analyzer as previously described [47]. The distribution of ion kinetic energies is nearly Gaussian with a FWHM between 0.2 and 0.4 eV (lab) for these experiments. The uncertainly in the absolute energy scale is ±0.05 eV (lab).

Pressure-dependent studies of the reaction cross-section are performed because multiple collisions can influence the shape of CID cross-sections and the threshold region is most sensitive to these effects. Data free from pressure effects are obtained by extrapolating to zero pressure of the neutral reactant, Xe, as previously described [48]. Results reported below are therefore the result of single bimolecular encounters.

2.2. Theoretical calculations

To obtain model structures, vibrational frequencies, rotational constants, and energetics for neutral indole, the various protonated tautomers of indole, and the transition states (TSs), intermediates (Ints), and products ($C_6H_5CH_2^+$ or $C_7H_7^+$ and HCN or HNC) involved in the activated dissociation of protonated indole and the isomerization of the dissociation products, theoretical calculations were performed using Gaussian 98 [49]. Geometry optimizations and frequency analyses were performed at the MPW1PW91/6-31G* level of theory [50]. The Cartesian coordinates of the MPW1PW91/6-31G* optimized geometries for all species computed are given in Supplementary Information, Table 1S. When used to model the data or to calculate zero point energy (ZPE) corrections, the MPW1PW91/6-31G* vibrational frequencies are pre-scaled by a factor of 0.948 [51]. The pre-scaled vibrational frequencies thus obtained for these systems are also listed in Supplementary Information, Table 2S, while rotational constants for the geometry optimized species are given in Table 3S. Single point energy calculations were performed at the MPW1PW91/6-311+G(2d,2p) and MP2(full)/6-311+G(2d,2p) levels using the MPW1PW91/6-31G* optimized geometries. ZPE and basis set superposition errors (BSSE) corrections are included in the calculated site-specific proton affinities and in relative energies of the dissociation products in the full counterpoise approximation [52,53]. These results are listed in Tables 1–4.

2.3. Thermochemical analysis

The threshold region of the CID cross-section of protonated indole is modeled using the following equation:

$$\sigma(E) = \frac{\sigma_0 \sum_i g_i (E + E_i - E_0)^n}{E} \quad (1)$$

where σ_0 is an energy-independent scaling factor, E the relative translational energy of the reactants, E_0 the threshold for reaction of the ground electronic and ro-vibrational state, and n is an adjustable parameter that describes the efficiency of collisional energy transfer [54]. The summation is over the ro-vibrational states of the reactant ions, i, where E_i is the excitation energy of each ro-vibrational state and g_i is the population of those states ($\Sigma g_i = 1$). The relative reactivity of all ro-vibrational states, as reflected by σ_0 and n, is assumed to be equivalent.

The Beyer–Swinehart algorithm [55] is used to evaluate the density of ro-vibrational states, and the relative populations,

Table 1
Site-specific proton affinities of indole at 0 K in kJ/mol

Site of protonation	MPW1PW91[a]			MP2(full)[b]			Literature values	
	Ee[a]	E_0[a,c]	$E_{0,BSSE}$[a,d]	Ee[b]	E_0[b,c]	$E_{0,BSSE}$[b,d]	Theory[e]	Experiment[f]
N1	867.3	832.6	831.5	851.2	816.5	807.5	823.0	
C2	899.2	868.9	868.1	857.3	827.0	819.2	869.0	
C3	924.3	892.8	892.2	900.4	868.9	861.0	888.7	933.4 (16.8)
C4	887.8	858.4	857.8	850.2	820.7	813.5	856.5	
C5	887.4	858.2	857.7	849.1	820.0	812.8	855.2	
C6	890.3	861.2	860.7	848.7	819.6	812.5	858.6	
C7	875.9	846.4	845.9	840.4	810.9	803.8	844.7	
C8	825.8	796.5	795.7	785.7	756.4	748.2	<795.0	
C9	825.5	797.2	796.5	787.0	758.7	750.6	<795.0	

[a] Calculated at the MPW1PW91/6-311+G(2d,2p)//MPW1PW91/6-31G* level of theory.
[b] Calculated at the MP2(full)/6-311+G(2d,2p)//MPW1PW91/6-31G* level of theory.
[c] Including ZPE corrections.
[d] Also includes BSSE corrections.
[e] Calculated at the B3LYP/6-31G*//B3LYP/6-31G* level including ZPE corrections [11].
[f] Ref. [58].

g_i, are calculated by an appropriate Maxwell–Boltzmann distribution at 298 K, the internal temperature of the reactants. The vibrational frequencies of protonated indole are determined from density functional theory calculations as discussed in Section 2.2. The average vibrational energy at 298 K of the various protonated indole tautomers, TSs, Ints, and products involved in the activated dissociation of protonated indole are given in Table 2S. Uncertainties in the vibrational energies are estimated by scaling the vibrational frequencies by ±10%. The corresponding change in the average vibrational energy is assumed to be an estimate of one standard deviation in the uncertainty in the vibrational energy, Table 2S.

Table 2
Relative stabilities (kJ/mol) of protonated indole and the transition states, intermediates, and products involved in the activated dissociation of protonated indole at 0 K

Species	MPW1PW91[a]		MP2(full)[b]	
	Ee[a]	E_0[a,c]	Ee[b]	E_0[b,c]
Indole_C3H$^+$	0.0	0.0	0.0	0.0
TS_{1A}, TS_{1B}	134.0	124.4	129.8	120.3
TS_{1C}	302.9	282.8	309.8	289.7
TS_{1D}	302.9	282.8	309.8	289.7
Int_{1A}, Int_{1B}	98.9	95.6	113.4	110.2
Int_{1C}	210.4	201.6	231.8	223.1
Int_{1D}	210.4	201.6	231.8	223.1
TS_{2A}, TS_{2B}	149.5	139.2	154.8	144.5
TS_{2C}	412.8	395.5	394.0	376.7
TS_{2D}	383.1	370.7	420.0	407.6
Int_{2A}, Int_{2B}	98.5	96.3	114.7	112.5
Int_{2C}	238.4	229.2	205.4	196.2
Int_{2D}	145.8	134.9	117.0	106.0
TS_{3A}, TS_{3B}	235.6	227.7	235.0	227.1
TS_{3D}	406.9	382.8	427.0	402.9
Int_{3A}, Int_{3B}	210.6	203.7	210.0	203.1
Int_{3D}	244.5	227.2	202.0	184.8
TS_{4A}	305.4	284.9	318.8	298.2
TS_{4B}	413.4	391.8	429.5	407.9
Int_{4A}	145.8	134.9	117.0	106.0
Int_{4B}	244.5	227.2	202.0	184.8
$C_6H_5CH_2^+$ + HNC	345.4	321.6	329.2	305.4
$C_6H_5CH_2^+$ + HCN	286.1	264.2	254.1	232.2

[a] Calculated at the MPW1PW91/6-311+G(2d,2p)//MPW1PW91/6-31G* level of theory.
[b] Calculated at the MP2(full)/6-311+G(2d,2p)//MPW1PW91/6-31G* level of theory.
[c] Including ZPE corrections.

Table 3
Relative stabilities (kJ/mol) of the transition states, intermediates, and products involved in the isomerization of $C_6H_5CH_2^+$ and $C_7H_7^+$ at 0 K

Species	MPW1PW91[a]		MP2(full)[b]	
	Ee[a]	E_0[a,c]	Ee[b]	E_0[b,c]
$C_6H_5CH_2^+$	0.0	0.0	0.0	0.0
TS_{1E}	424.8	407.5	451.8	434.5
TS_{1F}	245.0	236.1	259.7	250.8
Int_{1E}	179.0	179.0	102.8	102.7
Int_{1F}	227.8	219.1	236.2	227.5
TS_{2E}	253.2	244.5	250.0	240.9
TS_{2F}	285.3	271.7	299.5	285.9
$C_7H_7^+$	−42.7	−38.1	−46.7	−42.1

[a] Calculated at the MPW1PW91/6-311+G(2d,2p)//MPW1PW91/6-31G* level of theory.
[b] Calculated at the MP2(full)/6-311+G(2d,2p)//MPW1PW91/6-31G* level of theory.
[c] Including ZPE corrections.

Table 4
Relative stabilities (kJ/mol) of the transition states, intermediates, and products involved in the isomerization of HCN and HNC at 0 K

Species	MPW1PW91[a]		MP2(full)[b]	
	Ee[a]	E_0[a,c]	Ee[b]	E_0[b,c]
HNC	0.0	0.0	0.0	0.0
TS_{1G}	138.2	125.8	146.4	134.0
HCN	−59.3	−57.4	−75.1	−73.2

[a] Calculated at the MPW1PW91/6-311+G(2d,2p)//MPW1PW91/6-31G* level of theory.
[b] Calculated at the MP2(full)/6-311+G(2d,2p)//MPW1PW91/6-31G* level of theory.
[c] Including ZPE corrections.

The dissociation of ions becomes slower as the size of the reactant ion increases and as the critical energy needed to bring about dissociation increases. This leads to an increased probability that dissociation does not occur on the experimental time scale, $\sim 10^{-4}$ s for the experiments performed here. All CID processes that are faster than this are observed. However, as the lifetime of the energized ion approaches this limit, the apparent CID threshold shifts to higher energies, leading to a kinetic shift. The kinetic shift is quantified and corrected for in our analysis by including statistical theories for unimolecular dissociation, specifically Rice–Ramsperger–Kassel–Marcus (RRKM) theory, in Eq. (1) as described in detail elsewhere [42,56]. This requires sets of ro-vibrational frequencies appropriate for the energized ions and the transition states (TSs) leading to dissociation. In the present work, four distinct activated dissociation pathways (A–D) are computed for protonated indole, where each dissociation pathway is complex and involves multiple TSs and Ints. The rate of unimolecular dissociation of protonated indole is thus determined by the rate-limiting (highest energy) TS along the reaction pathway. This corresponds to a tight transition state (TTS) in all cases except dissociation pathway A computed at the MPW1PW91 level of theory, where the dissociation asymptote lies higher in energy than the highest energy TS. Thus, this latter dissociation pathway is also fit assuming a loose PSL TS model [42]. The molecular parameters of the reactant and rate-limiting TSs are derived from theoretical calculations as described in Section 2.2 and are summarized in Tables 2S and 3S.

Eq. (1) is convoluted with the kinetic and internal energy distributions of the reactants and a nonlinear least-squares analysis of the data is performed to give optimized values for the parameters σ_0, E_0, and n. Uncertainties in E_0 and E_0(TTS) or E_0(PSL) are determined from the range of threshold values for the eight zero-pressure-extrapolated data sets, variations associated with the vibrational frequencies (scaling as discussed above), and the error in the absolute energy scale, 0.05 eV (lab). For analyses that included the RRKM lifetime analysis, the uncertainties in the reported E_0(TTS) or E_0(PSL) values also include the effects of increasing and decreasing the time assumed available for dissociation by a factor of 2.

Eq. (1) explicitly includes the internal energy of the reaction ion, E_i. All energy available is treated statistically because the ro-vibrational energy of the reactant ion is redistributed throughout the ion upon impact with the collision gas, Xe. The threshold energies for the activated dissociation of protonated indole determined by analysis with Eq. (1), E_0(TTS), correspond to the activation energy, E_{act}, for this dissociation process at 0 K, while the E_0(PSL) threshold provides the ΔH_0 for activated dissociation of protonated indole.

3. Results

3.1. Cross-section for collision-induced dissociation

The experimental cross-section for the interaction of protonated indole with Xe is shown in Fig. 4. The only dissociation pathway observed over the range of collision energies examined here (0–12 eV) corresponds to elimination of HCN in the CID reaction 2.

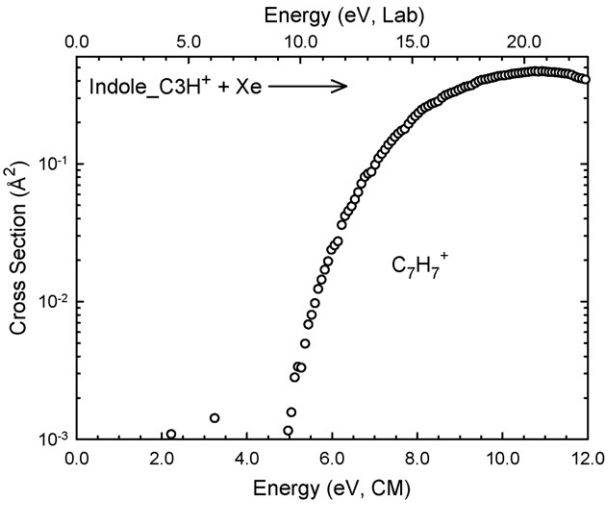

Fig. 4. Cross-section for the collision-induced dissociation of the protonated indole with Xe as a function of collision energy in the center-of-mass frame (lower *x*-axis) and laboratory frame (upper *x*-axis). Data for $(C_6H_5CH_2)^+$ product channel are shown for a Xe pressure of 0.2 mTorr.

$$H^+(\text{indole}) + Xe \rightarrow C_6H_5CH_2{}^+ + HCN + Xe \quad (2)$$

The $C_6H_5CH_2{}^+$ product cross-section slowly rises from an apparent threshold of ~4.9 eV to a maximum cross-section of ~0.5 Å^2 at a collision energy of 11 eV. The same reaction pathway was previously observed in high-energy collision activated dissociation (CAD) of protonated indole. However, under high-energy CAD conditions additional dissociation pathways become available to protonated indole and lead to a richer CAD spectrum [57]. Because the CID of protonated indole is only probed mass spectrometrically, it is unclear from the experimental data whether the products are formed as $C_6H_5CH_2{}^+$ or $C_7H_7{}^+$ and HCN or HNC. Thus, the theoretical results will be used to guide appropriate interpretation of the experimental data.

3.2. Theoretical results

Theoretical structures for neutral indole, the protonated tautomers of indole, and the transition states, intermediates, and products involved in the activated dissociation of protonated indole and isomerization of the dissociation products were calculated as described in Section 2.2. Energetics for these species were obtained from single point energy calculations at the MPW1MP91/6-311+G(2d,2p) and MP2(full)/6-311+G(2d,2p) levels of theory using the MPW1MP91/6-31G* optimized structures. The site-specific proton affinities (PAs) of indole are summarized in Table 1 along with calculated and measured values previously reported in the literature [11,58]. The relative stabilities of the ground state tautomer of protonated indole, and the transition states, intermediates, and products involved in the activated dissociation pathway to eliminate HCN (or HNC) are listed in Table 2. The potential energy landscapes including both optimized structures and the corresponding relative energies of the species involved in the activated dissociation of protonated indole are also shown in Figs. 5–8.

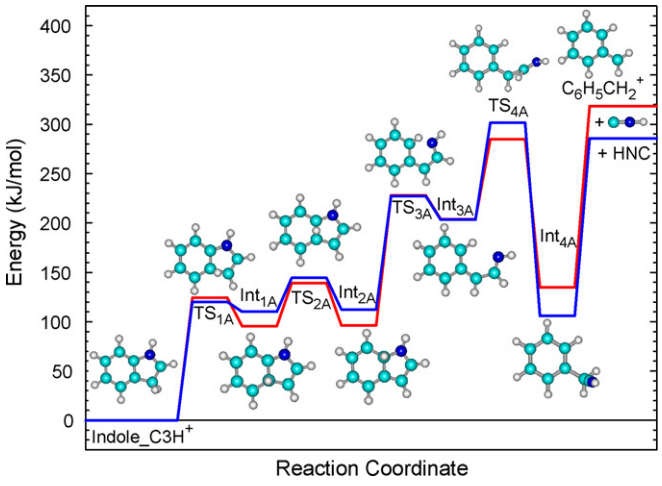

Fig. 5. Potential energy landscape at 0 K for pathway A leading to the elimination of HNC from protonated indole. Energies are relative to the reactant (C3-protonated indole), and taken from theoretical calculations at the MP2(full)/6-311+G(2d,2p) (blue line) and MPW1PW91/6-311+G(2d,2p) (red line) levels of theory using the MPW1PW91/6-31G* optimized geometries and including ZPE and BSSE corrections (Table 2).

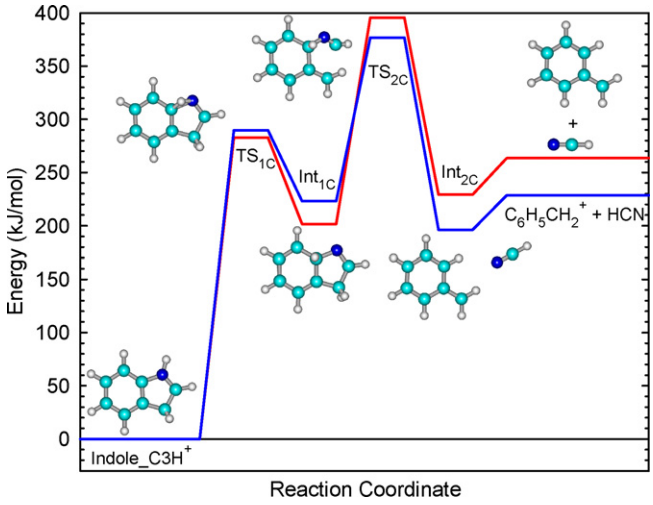

Fig. 7. Potential energy landscape at 0 K for pathway C leading to the elimination of HCN from protonated indole. Energies are relative to the reactant (C3-protonated indole), and taken from theoretical calculations at the MP2(full)/6-311+G(2d,2p) (blue line) and MPW1PW91/6-311+G(2d,2p) (red line) levels of theory using the MPW1PW91/6-31G* optimized geometries and including ZPE and BSSE corrections (Table 2).

3.2.1. Site-specific proton affinities of indole

The MPW1MP91/6-311+G(2d,2p) and MP2(full)/6-311+G(2d,2p) calculated site-specific PAs of indole are listed in Table 1. Stable proton binding modes are found for all ring sites, N1 and C2–C9. In all cases the absolute PAs calculated at the MPW1PW91 level of theory exceed the MP2 values. The average difference in the MPW1PW91 and MP2 PAs is 41.9 ± 8.6 kJ/mol. In contrast, the relative site-specific PAs determined using these theories are very parallel for all sites except N1 and C3, where smaller differences in the computed MPW1PW91 and MP2(full) PAs are found for the N1 and C3 sites, 24.0 and 31.2 kJ/mol, respectively. When these two values are excluded, the average difference in the computed PAs is slightly larger, while the standard deviation is smaller, 46.0 ± 2.4 kJ/mol. Although the absolute and relative PAs differ somewhat between these two levels of theory, both find that the most favorable site for proton binding is at the C3 position. In addition, the PAs of the other sites in indole are calculated to be at least 24.1 kJ/mol less favorable than C3. Thus, only the C3 protonated tautomer of indole tautomer should be generated under the experimental conditions employed here.

3.2.2. Potential energy landscapes for activated dissociation of protonated indole

As discussed above, only a single activated dissociation pathway is observed in the low-energy CID of protonated indole.

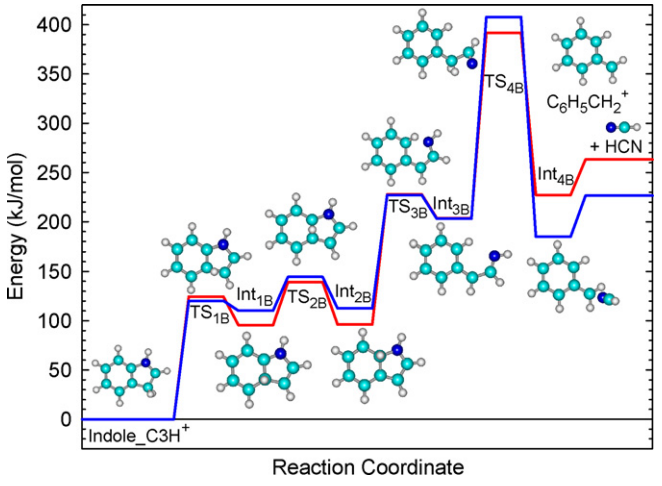

Fig. 6. Potential energy landscape at 0 K for pathway B leading to the elimination of HCN from protonated indole. Energies are relative to the reactant (C3-protonated indole), and taken from theoretical calculations at the MP2(full)/6-311+G(2d,2p) (blue line) and MPW1PW91/6-311+G(2d,2p) (red line) levels of theory using the MPW1PW91/6-31G* optimized geometries and including ZPE and BSSE corrections (Table 2).

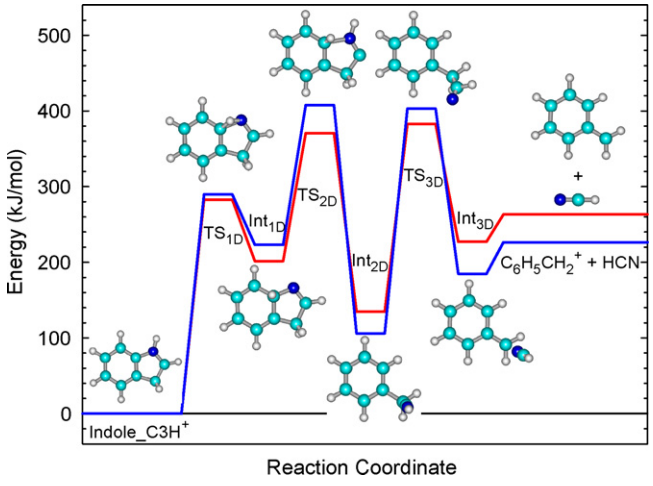

Fig. 8. Potential energy landscape at 0 K for pathway D leading to the elimination of HCN from protonated indole. Energies are relative to the reactant (C3-protonated indole), and taken from theoretical calculations at the MP2(full)/6-311+G(2d,2p) (blue line) and MPW1PW91/6-311+G(2d,2p) (red line) levels of theory using the MPW1PW91/6-31G* optimized geometries and including ZPE and BSSE corrections (Table 2).

To allow appropriate thermochemical analysis of the experimentally measured cross-section, the structures and molecular parameters of the reactant ion and the rate-limiting TS leading to dissociation must be determined. The calculated site-specific proton affinities of indole indicate that the C3 protonated tautomer of indole is the most stable and thus its molecular parameters are used to describe the reactant ion. To determine the structure of the rate-limiting TS, we have also mapped out four distinct theoretical potential energy landscapes for the unimolecular dissociation of protonated indole as summarized in Table 2 and shown in Figs. 5–8. In all cases, the activated dissociation of protonated indole is complex and found to involve several sequential steps.

3.2.2.1. Activated dissociation of protonated indole: pathway A. The activated dissociation of protonated indole along pathway A is shown in Fig. 5. The first step along the reaction coordinate involves proton-transfer isomerization, where the excess proton migrates from the C3 to the C9 position via TS_{1A} to produce Int_{1A}. The second step also involves proton-transfer isomerization, where the proton migrates from the C9 to the C8 position via TS_{2A} to produce Int_{2A}. The third step involves N1–C8 bond cleavage resulting in opening of the pyrrolyl ring of indole via TS_{3A} to produce Int_{3A}. The fourth step involves proton transfer from C3 to C2 via TS_{4A} to produce Int_{4A}. Int_{4A} dissociates smoothly into $C_6H_5CH_2^+$ and HNC upon cleavage of the C2–C3 bond with no barrier in excess of the endothermicity of dissociation, as shown in the relaxed potential energy scan of Fig. 9.

As can be seen in Fig. 5, the MPW1PW91 and MP2 computational methods give very similar shapes for the potential energy landscape. However, MP2 results suggest that Int_{1A}, Int_{2A}, and TS_{4A} are less stable, while Int_{4A} and the products are more stable than found using MPW1PW91 theory. Most significantly the MP2 activation energy is 13.3 kJ/mol larger, while the enthalpy of dissociation is 32.7 kJ/mol lower than found at the MPW1PW91 level of theory.

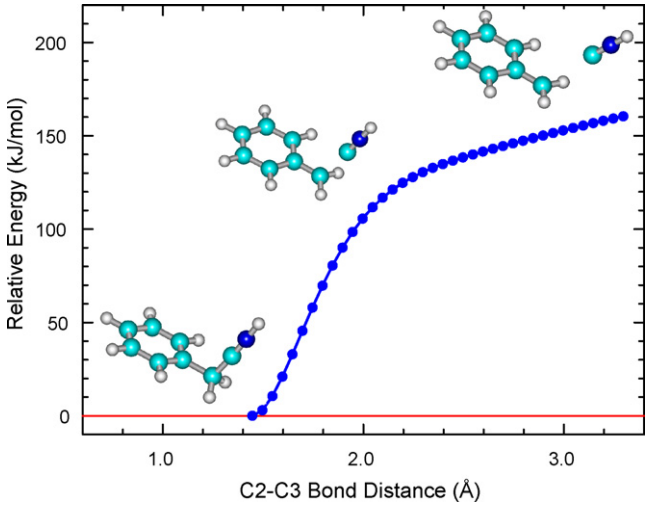

Fig. 9. Relaxed potential energy scan at 0 K for dissociation of Int_{4A} along the C2–C3 bond. Energies are relative to Int_{4A}, and taken from theoretical calculations at the MPW1PW91 level of theory.

3.2.2.2. Activated dissociation of protonated indole: pathway B. The activated dissociation of protonated indole along pathway B is shown in Fig. 6. The first three steps along this dissociation pathway are the same as that found for pathway A (i.e., the first three TSs and Ints are the same). Dissociation pathway B differs from pathway A in that the fourth step involves proton transfer from N1 to C3 followed by cleavage of the C2–C3 bond via TS_{4B} to produce Int_{4B}. Because Int_{4B} is a simple electrostatically bound ion–molecule complex between $C_6H_5CH_2^+$ and HCN it dissociates smoothly to the products via a loose TS with no barrier in excess of the endothermicity of dissociation. Thus, the ionic product formed along pathway B is the same as that found for pathway A, $C_6H_5CH_2^+$, however, the neutral product differs, and is HCN rather than HNC. As can been seen in Fig. 6, the MPW1PW91 and MP2 computational methods again give similar shapes to the potential energy landscape. However, MP2 results suggest that Int_{1B}, Int_{2B}, and TS_{4B} are less stable, while Int_{4B} and the products are more stable than found using MPW1PW91 theory. Similar to that found for pathway A, the MP2 activation energy is larger than found at the MPW1PW91 level of theory, by 16.1 kJ/mol.

3.2.2.3. Activated dissociation of protonated indole: pathway C. The activated dissociation of protonated indole along pathway C is shown in Fig. 7. The first step along the reaction coordinate involves proton-transfer isomerization, where the proton migrates from the N1 to the C8 position via TS_{1C} to produce Int_{1C}. The second step involves C2–C3 bond cleavage resulting in opening of the pyrrolyl ring of indole via TS_{2C}, followed by N1–C8 bond cleavage to produce Int_{2C}. Int_{2C} is again a simple electrostatically bound ion–molecule complex between $C_6H_5CH_2^+$ and HCN and dissociates to the products via a loose TS with no barrier in excess of the endothermicity of dissociation. While the energetics for pathway C differs from that found for B, both the ionic and neutral products formed along these dissociation pathways are the same.

As can be seen in Fig. 7, the MPW1PW91 and MP2 computational methods again give very similar shapes for the potential energy landscape. However, MP2 results suggest that TS_{1C} and Int_{1C} are less stable, while TS_{2C}, Int_{2C}, and the products are more stable than found using MPW1PW91 theory. In contrast to that found for pathways A and B, the MP2 activation energy is 18.8 kJ/mol lower than found at the MPW1PW91 level of theory.

3.2.2.4. Activated dissociation of protonated indole: pathway D. The activated dissociation of protonated indole along pathway D is shown in Fig. 8. The first step along this dissociation pathway is the same as that found for pathway C (i.e., the first TS and Int are the same). The second step involves proton migration from C2 to N1, resulting in lengthening of the N1–C8 bond via TS_{2D}, followed by cleavage of the N1–C8 bond resulting in opening of the pyrrolyl ring of indole to produce Int_{2D}. The third step involves proton transfer from N1 to C2 via TS_{3D}, followed by C2–C3 bond cleavage to produce Int_{3D}. Int_{3D} is again a simple electrostatically bound ion–molecule complex between $C_6H_5CH_2^+$ and HCN and dissociates to the products via a loose TS with no barrier in excess of the endothermicity

of dissociation. Again, although the energetics for pathway D differs from that found for B and C, both the ionic and neutral products formed along these three pathways are the same.

As can be seen in Fig. 8, the MPW1PW91 and MP2 computational methods give very similar shapes for the potential energy landscape. However, MP2 results suggest that TS_{1D}, TS_{2D}, TS_{3D} and Int_{1D} are less stable, while Int_{2D}, Int_{3D}, and the products are more stable than found using MPW1PW91 theory. Both theories find similar energies for TS_{2D} and TS_{3D}. However, MPW1PW91 theory suggests that TS_{3D} is the rate-limiting TS, while MP2 theory suggests that TS_{2D} is rate limiting. As found for pathways A and B, the MP2 activation energy is 24.8 kJ/mol larger than found at the MPW1PW91 level of theory.

The potential energy landscapes computed here for the dissociation of protonated indole suggest that the ionic product initially formed is always $C_6H_5CH_2^+$, while the neutral product is HNC along one pathway, and HCN for the three other pathways. However, the initial products may be formed with enough internal energy to isomerize. Thus potential energy landscapes for the isomerization of both the ionic ($C_6H_5CH_2^+$ to $C_7H_7^+$) and neutral products (HCN and HNC) were also computed.

3.2.2.5. Isomerization of the ionic product ($C_6H_5CH_2^+$ versus $C_7H_7^+$). Both MPW1PW91 and MP2 theories find that the benzyl cation, $C_6H_5CH_2^+$, is less stable than the tropyllium cation, $C_7H_7^+$, by 38.1 and 42.1 kJ/mol, respectively. Thus, the isomerization of the initially formed $C_6H_5CH_2^+$ should be thermodynamically favorable so long as it is formed with sufficient internal energy to undergo isomerization. We found two distinct pathways for isomerization of $C_6H_5CH_2^+$ and $C_7H_7^+$ (Table 3 and Figs. 10 and 11). The isomerization of $C_6H_5CH_2^+$ along pathway E is shown in Fig. 10. The first step involves insertion of the benzyl CH_2 group into the ring via TS_{1E} to produce Int_{1E}. In the second step, Int_{1E} undergoes a change in conformation followed by proton-transfer isomerization from the CH_2 moiety

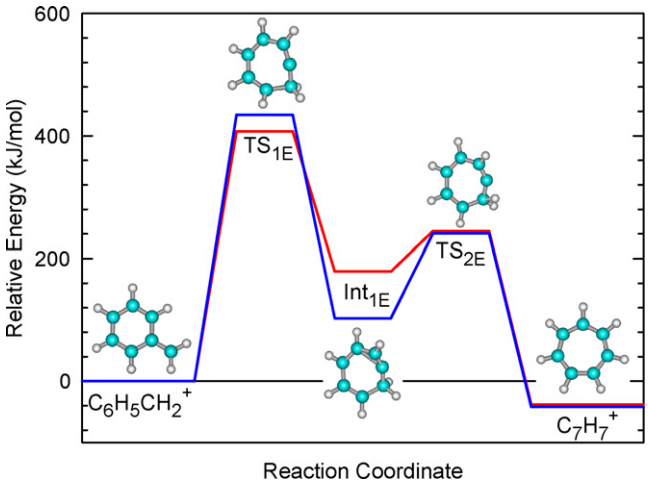

Fig. 10. Potential energy landscape at 0 K for pathway E leading to the isomerization of $C_6H_5CH_2^+$ and $C_7H_7^+$. Energies are relative to the $C_6H_5CH_2^+$ moiety, and taken from theoretical calculations at the MP2(full)/6-311+G(2d,2p) (blue line) and MPW1PW91/6-311+G(2d,2p) (red line) levels of theory using the MPW1PW91/6-31G* optimized geometries and including ZPE corrections (Table 3).

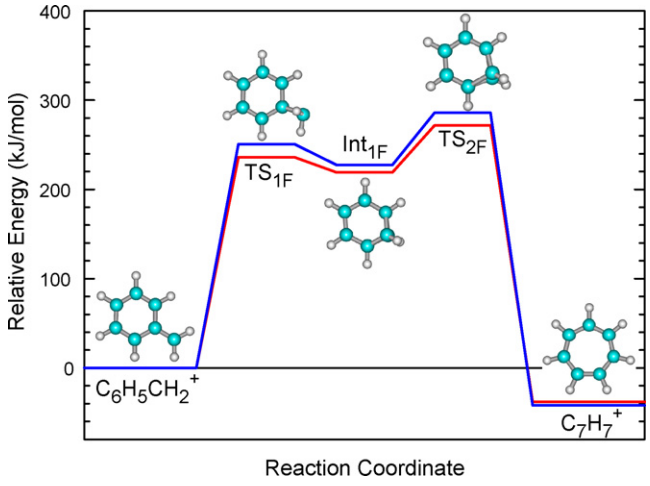

Fig. 11. Potential energy landscape at 0 K for pathway F leading to the isomerization of $C_6H_5CH_2^+$ and $C_7H_7^+$. Energies are relative to the $C_6H_5CH_2^+$ moiety, and taken from theoretical calculations at the MP2(full)/6-311+G(2d,2p) (blue line) and MPW1PW91/6-311+G(2d,2p) (red line) levels of theory using the MPW1PW91/6-31G* optimized geometries and including ZPE corrections (Table 3).

to the adjacent carbon having no hydrogen atoms attached via TS_{2E} to produce $C_7H_7^+$. TS_{1E} is found to be the rate-limiting TS and lies 407.5 and 434.5 kJ/mol above the $C_6H_5CH_2^+$ moiety at the MPW1PW91 and MP2 levels of theory, respectively. The isomerization of $C_6H_5CH_2^+$ along pathway F is shown in Fig. 11. The first step involves proton migration from the CH_2 moiety to C1 via TS_{1F} resulting in insertion of the CH into a symmetric bis-six-membered ring structure, Int_{1F}. This intermediate distorts to accommodate insertion of both CH groups into a single seven-membered ring via TS_{2F} to produce $C_7H_7^+$. TS_{2F} is found to be the rate-limiting TS along pathway F and lies 271.7 and 285.9 kJ/mol above the $C_6H_5CH_2^+$ moiety at the MPW1PW91 and MP2 levels of theory, respectively. Therefore, pathway F is energetically favored over pathway E. The computed AEs for the isomerization of $C_6H_5CH_2^+$ exceed the difference in energy between the rate-limiting TS and the dissociation products for all four dissociation pathways computed. Thus, at threshold the $C_6H_5CH_2^+$ product ion will not have sufficient internal energy to isomerize. However, at sufficiently high collision energies, isomerization may occur.

3.2.2.6. Isomerization of the neutral product (HCN versus HNC). Both MPW1PW91 and MP2 theories find that HNC is less stable than HCN, by 57.4 and 73.2 kJ/mol, respectively. Thus, the isomerization of the initially formed HNC along pathway A should be thermodynamically favorable so long as it is formed with sufficient internal energy to undergo isomerization. The isomerization of HCN and HNC along pathway G is summarized in Table 4 and shown in Fig. 12. The isomerization is a single step process involving proton migration between the C and N atoms via TS_{1G}. TS_{1G} lies 125.8 and 134.0 kJ/mol above the HNC moiety, and 183.2 and 207.2 kJ/mol above the HCN moiety at the MPW1PW91 and MP2 levels of theory, respectively. Again, the computed AEs for the isomerization of HNC and HCN exceed the difference in energy between the rate-limiting

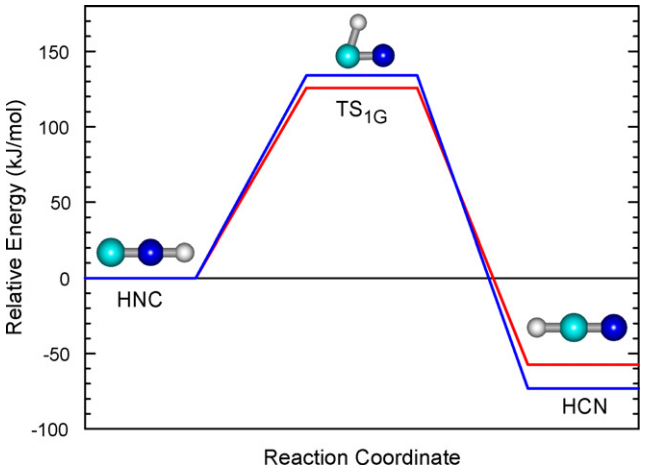

Fig. 12. Potential energy landscape at 0 K for pathway G leading to the isomerization of HNC and HCN. Energies are relative to the HNC moiety, and taken from theoretical calculations at the MP2(full)/6-311+G(2d,2p) (blue line) and MPW1PW91/6-311+G(2d,2p) (red line) levels of theory using the MPW1PW91/6-31G* optimized geometries and including ZPE corrections (Table 4).

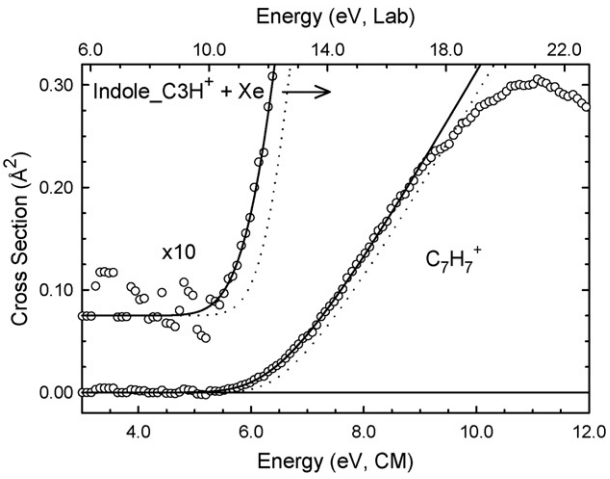

Fig. 13. Zero-pressure-extrapolated cross-section for collision-induced dissociation of protonated indole with Xe in the threshold region as a function of kinetic energy in the center-of-mass frame (lower *x*-axis) and laboratory frame (upper *x*-axis). The solid line shows the best fit to the data using a TTS model (based on the calculated rate-limiting TS_{4B}) convoluted over the neutral and ion kinetic and internal energy distributions. The dashed line shows the model cross-sections in the absence of experimental kinetic energy broadening for reactants with an internal energy corresponding to 0 K.

TS and the dissociation products for all four dissociation pathways computed. Thus, at threshold the HNC (HCN) product will not have sufficient internal energy to isomerize. However, at sufficiently high collision energies, isomerization may occur.

3.3. Threshold analysis

The threshold region for reaction 2 in protonated indole was analyzed along each of the four dissociation pathways computed using the model of Eq. (1). The results of these analyses are summarized in Table 5. In all cases, good reproduction of the data is obtained over an energy range extending up to 9.0 eV. A threshold energy of 6.10 ± 0.22 eV is determined when RRKM lifetime effects are not included. The threshold energies determined when lifetime effects are included are sensitive to the TS used to model the data, and vary between 3.72 ± 0.14 and 4.17 ± 0.16 eV for the various TTS models, and is much larger for the loose PSL TS model, 4.84 ± 0.15 eV The zero-pressure-extrapolated CID cross-section and fit to the experimental data using a TTS model corresponding to pathway B for the interaction of protonated indole with Xe is shown in Fig. 13, results for all other fits are very similar. Previous work has shown that such a TTS model provides an accurate assessment of the kinetic shift and threshold energy for CID processes that involve covalent bond cleavage/formation reactions in which TTSs are involved [43,44]. Similarly, previous work has shown that a loose PSL TS model provides the most accurate assessment of the kinetic shift and threshold energy for CID processes that involve simple bond cleavage reactions that exhibit no barrier in excess of the endothermicity of dissociation [42]. Thus, dissociation of protonated indole exhibits a large kinetic shift in excess of 1.26 eV.

3.3.1. Threshold analysis along pathway A

Both MPW1PW91 and MP2(full) theories find that TS_{4A} exhibits the largest barrier. However, MPW1PW91 theory suggests that this barrier lies below the $C_6H_5CH_2^+$ and HNC dissociation asymptote. Thus, based upon dissociation pathway A, the experimental data was fit in two different ways. In the first case, it is assumed that TS_{4A} lies below the dissociation asymptote as found by MPW1PW91 theory, and the data is fit using a loose PSL TS model. In the second case, it is assumed that TS_{4A} lies above the dissociation asymptote as found by

Table 5
Fitting parameters of Eq. (1), threshold dissociation energies at 0 K, and entropies of activation at 1000 K of protonated indole[a]

Species	σ_0	n	E_0 (eV)	Kinetic shift (eV)	$\Delta S^{\dagger}$(TS) (J K^{-1} mol^{-1})
No RRKM analysis	0.4 (0.1)	1.4 (0.1)	6.10 (0.22)	–	–
Pathway A, PSL TS	0.5 (0.1)	1.4 (0.1)	4.84 (0.15)	1.26	111.6 (4.7)
Pathway A, TS_{4A} TTS	0.6 (0.1)	1.3 (0.1)	3.99 (0.13)	2.11	3.4 (0.2)
Pathway B, TS_{4B} TTS	0.6 (0.1)	1.2 (0.1)	3.83 (0.14)	2.27	8.1 (0.6)
Pathway C, TS_{2C} TTS	0.6 (0.1)	1.2 (0.1)	3.80 (0.16)	2.30	20.5 (0.5)
Pathway D, TS_{3D} TTS	0.5 (0.1)	1.4 (0.1)	4.17 (0.16)	1.93	55.1 (0.3)
Pathway D, TS_{2D} TTS	0.7 (0.2)	1.2 (0.1)	3.72 (0.14)	2.38	6.3 (0.6)

[a] Uncertainties are listed in parentheses.

MP2 theory, and is therefore the rate-determining step for activated dissociation of protonated indole. Thus, a TTS based upon TS_{4A} is also used to model the experimental data. As can be seen in Table 5, fits to the data using a loose PSL model provide a threshold energy of 4.84 ± 0.15 eV, while the TTS model using the parameters of TS_{4A} determine a much lower threshold of 3.99 ± 0.13 eV.

3.3.2. Threshold analysis along pathway B

Both MPW1PW91 and MP2(full) theories find that TS_{4B} exhibits the largest barrier. As the highest energy barrier, TS_{4B} is the rate-determining step for activated dissociation of protonated indole. In addition, TS_{4B} lies higher in energy than the dissociation products. Therefore, the molecular parameters of TS_{4B} are used to model the TS to correct for the kinetic shift in the measured cross-section. As summarized in Table 5, a fit to the experimental data using a TTS model based upon TS_{4B} provides a threshold energy of 3.83 ± 0.14 eV.

3.3.3. Threshold analysis along pathway C

Both MPW1PW91 and MP2(full) theories find that TS_{2C} exhibits the largest barrier. In addition, this TS lies higher in energy than the dissociation products. Thus, based upon dissociation pathway C, the experimental data was fit using a TTS based upon TS_{2C}. As summarized in Table 5, a fit to the experimental data using this model provides a threshold energy of 3.80 ± 16 eV.

3.3.4. Threshold analysis along pathway D

MPW1PW91 theory finds that TS_{3D} exhibits the largest barrier, while MP2 theory suggest that TS_{2D} exhibits the largest barrier. In both cases, these TSs lie higher in energy than the dissociation products. Thus, based upon dissociation pathway D, the experimental data was fit using a TTS based upon both TS_{2D} and TS_{3D}. As summarized in Table 5, fits to the experimental data based upon TS_{2D} and TS_{3D} determined threshold energies of 3.72 ± 0.14 and 4.17 ± 0.16 eV, respectively.

3.3.5. Entropy of activation

The entropy of activation, $\Delta S^{\dagger}$ is a measure of the tightness (looseness) of the TS and also a reflection of the complexity of the system. It is determined from the molecular parameters used to model the energized ion and TS for dissociation, but also depends upon the threshold energy. The $\Delta S^{\dagger}$(TS) at 1000 K determined for the dissociation of protonated indole varies with the TS used to model the data. When a TTS model is used, $\Delta S^{\dagger}$(TS) is smaller and varies between 3.4 and 55.1 J K^{-1} mol^{-1}. In contrast, a much larger $\Delta S^{\dagger}$(TS) is found for the loose PSL TS model, 111.6 J K^{-1} mol^{-1}, as expected.

3.3.6. Conversion from 0 to 298 K

To allow comparison to commonly employed experimental conditions, we convert the 0 K measured and calculated activation energies determined here to 298 K activation enthalpies and free energies [42]. The enthalpy and entropy conversions are

Table 6
Activation energies at 0 and 298 K and activation free energies at 298 K for activated dissociation of protonated indole resulting in elimination of HCN in kJ/mol[a]

Method	ΔH_0	$\Delta H_{298} - \Delta H_0$	ΔH_{298}	$T\Delta S_{298}$	ΔG_{298}
Pathway A, Indole_C3H$^+$ → $C_6H_5CH_2^+$ + HNC, PSL TS					
TCID	467.0 (14.5)	8.0 (1.0)	475.0 (14.5)	47.7 (0.2)	427.3 (14.5)
MPW1PW91	318.3	8.0 (1.0)	326.3	47.7 (0.2)	278.6
MP2	285.6	8.0 (1.0)	293.6	47.7 (0.2)	245.9
Pathway A, Indole_C3H$^+$ → $C_6H_5CH_2^+$ + HNC, TS_{4A} TTS					
TCID	384.8 (12.9)	5.8 (0.7)	390.6 (12.9)	2.7 (1.8)	387.9 (13.0)
MPW1PW91	284.9	5.8 (0.7)	290.7	2.7 (1.8)	288.0
MP2	298.2	5.8 (0.7)	304.0	2.7 (1.8)	301.3
Pathway B, Indole_C3H$^+$ → $C_6H_5CH_2^+$ + HCN, TS_{4B} TTS					
TCID	369.7 (13.3)	3.7 (2.7)	373.4 (13.6)	1.7 (0.8)	371.7 (13.6)
MPW1PW91	391.8	3.7 (2.7)	395.5	1.7 (0.8)	393.8
MP2	407.9	3.7 (2.7)	411.6	1.7 (0.8)	409.9
Pathway C, Indole_C3H$^+$ → $C_6H_5CH_2^+$ + HCN, TS_{2C} TTS					
TCID	366.6 (15.4)	4.6 (0.5)	371.2 (15.4)	0.1 (0.3)	371.1 (15.4)
MPW1PW91	395.5	4.6 (0.5)	400.1	0.1 (0.3)	400.0
MP2	376.7	4.6 (0.5)	381.3	0.1 (0.3)	381.2
Pathway D, Indole_C3H$^+$ → $C_6H_5CH_2^+$ + HCN, TS_{3D} TTS					
TCID	402.4 (15.4)	7.4 (2.8)	409.8 (15.7)	6.9 (2.7)	402.9 (15.9)
MPW1PW91	382.8	7.4 (2.8)	390.2	6.9 (2.7)	383.3
MP2	402.9	7.4 (2.8)	410.3	6.9 (2.7)	403.4
Pathway D, Indole_C3H$^+$ → $C_6H_5CH_2^+$ + HCN, TS_{2D} TTS					
TCID	358.9 (13.5)	7.4 (2.8)	366.3 (13.8)	6.9 (2.7)	359.4 (14.0)
MPW1PW91	370.7	7.4 (2.8)	378.1	6.9 (2.7)	371.2
MP2	407.6	7.4 (2.8)	415.0	6.9 (2.7)	408.1

Thermal corrections computed at the MPW1PW91/6-31G* level with frequencies scaled by 0.948. Uncertainties in the enthalpic and entropic corrections are determined by 10% variation in the molecular constants, and a factor of two in the frequencies below 150 cm^{-1}.

[a] Uncertainties are listed in the parentheses.

calculated using standard formulas (assuming harmonic oscillator and rigid rotor modes) and the vibrational and rotational constants determined for the MPW1PW91 optimized geometries. Table 6 list the 0 and 298 K enthalpy, free energy, and enthalpic and entropic corrections for the various dissociation pathways computed. Uncertainties in the enthalpic and entropic corrections are determined by 10% variation in the molecular constants.

4. Discussion

4.1. Comparison of theory and experiment

The present results are the first direct measurement of the activation energy for elimination of HCN (or HNC) from protonated indole. The threshold energy determined for this activated dissociation pathway is sensitive to the model employed to describe the rate-limiting TS. Thus, the results obtained based upon each model are discussed independently.

4.1.1. Dissociation pathway A

When the PSL TS model is used to fit the experimental data, a threshold energy of 467.0 ± 14.5 kJ/mol is obtained. When modeled in this fashion, the threshold energy should correspond to the enthalpy of dissociation, which is computed to be 318.3 and 285.6 kJ/mol, at the MPW1PW91 and MP2 levels of theory, respectively. A much smaller threshold of 384.8 ± 12.9 kJ/mol is determined when a TTS model based upon TS_{4A} is used. In this case, the threshold energy should correspond to the activation energy for dissociation, which is computed to be 284.9 and 298.2 kJ/mol at the MPW1PW91 and MP2 levels of theory, respectively. In either case, the threshold energies determined significantly exceed the computed values, suggesting that theory significantly underestimates the activation energy for loss of HCN along pathway A.

4.1.2. Dissociation pathway B

When a TTS model based upon TS_{4B} is used to model the experimental data, a threshold energy of 369.7 ± 13.3 kJ/mol is obtained. This compares reasonably well with the MPW1PW91 and MP2 activation energies of 391.8 and 407.9 kJ/mol. The difference in the measured and computed values, 22.1 and 38.2 kJ/mol, respectively is larger than the experimental uncertainty, suggesting that if dissociation occurs along pathway B that a somewhat higher level of theory is needed to accurately describe the rate-limiting transition state, TS_{4B}.

4.1.3. Dissociation pathway C

When a TTS model based upon TS_{2C} is used to model the experimental data, a threshold energy of 366.6 ± 15.4 kJ/mol is obtained. This compares reasonably well with the MPW1PW91 and MP2 activation energies of 395.5 and 376.7 kJ/mol. The difference in the measured and computed values is 28.9 and 10.1 kJ/mol, respectively. While the MPW1PW91 value still lies outside of the experimental uncertainty, the MP2 value agrees quite nicely. This suggests that if dissociation occurs along pathway C that MP2 performs quite well, but that a somewhat larger basis set is needed with the MPW1PW91 level of theory to accurately describe the rate-limiting transition state, TS_{2C}.

4.1.4. Dissociation pathway D

When a TTS model based upon TS_{3D} is used to model the experimental data, a threshold energy of 402.4 ± 15.4 kJ/mol is obtained. This compares reasonably well with the MPW1PW91 and MP2 activation energies of 382.8 and 402.9 kJ/mol. The difference in the measured and computed values is 19.6 and 0.5 kJ/mol, respectively. While the MPW1PW91 value still lies outside of the experimental uncertainty, the MP2 value is in excellent agreement. When a TTS model based upon TS_{2D} is used to model the experimental data, a threshold energy of 358.9 ± 13.5 kJ/mol is obtained. This again compares reasonably well with the MPW1PW91 and MP2 activation energies of 370.7 and 407.6 kJ/mol. The difference in the measured and computed values is 11.8 and 48.7 kJ/mol, respectively. Now, the MPW1PW91 value is in good agreement with the measured value, whereas the agreement for MP2 is rather poor. Thus the agreement between theory and experiment is good to excellent when TS_{3D} is used to model the data, and somewhat less satisfactory when TS_{2D} is used, suggesting that TS_{3D} is the rate-limiting TS as suggested by MPW1PW91 theory.

Overall, it is clear that although pathway A is computed to provide the lowest-energy pathway to dissociation, the energetics do not exhibit reasonable agreement with the experimental results. In contrast, pathways B–D all exhibit reasonable agreement. Thus, the present results suggest that protonated indole dissociates to produce $C_6H_5CH_2^+$ and HCN at threshold.

4.2. Comparison with literature results

4.2.1. Site-specific proton affinities of indole

The protonation of indole was investigated in an earlier theoretical study [11]. Site-specific PAs were calculated for all possible sites of indole at the B3LYP/6-31G* level of theory with geometries optimized and ZPE corrections computed at the same level of theory. In agreement with the present results, C3 was found to be the most favorable proton-binding site. The MPW1PW91/6-311+G(2d, 2p) and B3LYP/6-31G* values are virtually identical, with a mean absolute deviation (MAD) of 2.9 ± 2.6 kJ/mol (for proton binding at N1 and C2–C7 as only upper limits to the PAs at C8 and C9 were estimated), while the MP2(full) values are lower but parallel the density functional PAs. The largest deviation between the MPW1PW91 and B3LYP values is found for the N1 proton affinity of indole, 8.5 kJ/mol. When the N1 PA is not included, the MAD between MPW1PW91 and B3LYP PAs reduces to 1.9 ± 1.0 kJ/mol. It is interesting to note that the estimated upper limits for the PAs at C8 and C9 are nearly equal to the MPW1PW91 PAs, indicating that the estimated upper limits are very good estimates. The measured PA of indole, 933.4 ± 16.8 kJ/mol [11,58] is larger than the B3LYP [11], MPW1PW91, and MP2(full) calculated values. Better agreement is found with the MPW1PW91 (892.2 kJ/mol) and B3LYP (888.7 kJ/mol) values than for MP2(full) theory (861.0 kJ/mol). The differences in the measured and calculated PAs are larger than the experimental error in the measured PA,

and suggest that a somewhat higher level of theory is needed to accurately describe the structure and energetics of indole and protonated indole.

In a previous study it was shown that in aqueous solution protonation of indole occurs at the N1, C2, and C3 positions with the C3-protonated tautomer being the most favorable and predominant species present [59]. In contrast, the calculated gas phase PAs for protonation at N1 and C2 are 60.7 and 24.1 kJ/mol lower than the C3 PA using MPW1PW91 theory. Similarly, the N1 and C2 PAs are 53.5 and 41.8 kJ/mol lower than the C3 PA using MP2(full) theory. Because a Maxwell–Boltzmann distribution at 298 K should be generated in our experiments, the C3-protonated tautomer of indole should be the only form produced in measurable quantities (>99.9%). Previous experimental studies compared the CAD spectra of independently generated C3-protonated indole by various methods with the $C_8H_8N^+$ ions obtained by protonation of indole. The resulting CAD spectra were almost identical, indicating that protonation of indole occurs solely at the C3 position in the gas phase [57] in agreement with the present theoretical results.

4.2.2. *Potential energy landscape for activated dissociation of protonated indole*

An earlier collision activation dissociation (CAD) study of protonated indole suggested a possible mechanism for HCN elimination via an open-chain intermediate [57]. An approximate potential energy profile for the reaction was also generated. The overall rate-limiting step was believed to involve ring opening of the heterocyclic counterpart of protonated indole. The energy barrier for this process was estimated to be >299.0 kJ/mol. For the three dissociation pathways leading to elimination of HCN, B, C, and D, the ring-opening step is only rate limiting for pathways C and D at the MPW1PW91 level of theory. However in all cases, the rate-limiting TS exceeds the lower bound previously estimated. The measured activation energies along these pathways are also quite large and in excess of 350 kJ/mol. Thus, the theoretical calculations performed here predict a different rate-limiting TS and both theoretical and experimental results indicate that the barrier to activated dissociation of protonated indole is much higher in energy than the lower bound previously estimated [57].

5. Conclusions

The kinetic energy dependence of the collision-induced dissociation of protonated indole with Xe is examined in a guided ion beam mass spectrometer. The only dissociation process observed is loss of neutral HCN (or HNC). The threshold for this process is determined after consideration of the effects of the internal energy distribution of the reactant ions, multiple collisions with Xe, and lifetime effects (using methodology described in detail elsewhere) [42–44]. The site-specific proton affinities of indole are calculated for all possible proton-binding sites. The results indicate that the most favorable site for protonation is at C3. Energetics and insight into the structures of the species involved in the activated dissociation of protonated indole and theoretical estimates for the potential energy landscape and activation energy are provided by theoretical calculations of the relevant species at the MPW1PW91/6-311+G(2d,2p) and MP2(full)/6-311+G(2d,2p) levels of theory using the MPW1PW91/6-31G* optimized geometries. The vibrational frequencies and rotational constants of the reactant (C3-protonated indole) and rate-determining transition states (PSL, TS_{4A}, TS_{4B}, TS_{2C}, TS_{3D}, and TS_{2D}) are used for thermodynamic analysis of the experimental data. The experimental threshold activation energies determined here exhibit very poor agreement with the theoretical values derived from MPW1PW91 and MP2 theories along pathway A. Thus, it appears that theory significantly underestimates the activation energy required for elimination of HNC. In contrast, the experimental threshold activation energies determined here are in reasonable agreement with values derived for pathways B–D. MPW1PW91 theory suggests that pathway D is most favorable, while MP2 suggests that pathway C is the most favorable. Because definitive conclusions about the accuracy of the computed dissociation pathways cannot be assessed based upon the present results, a best estimate for the activation energy of protonated indole (corresponding to the average of the threshold energies obtained along these pathways) of 374.4 ± 29.8 kJ/mol is recommended.

Acknowledgements

This work is supported by the National Science Foundation, Grant CHE-0518262 and the American Chemical Society Petroleum Research Fund, Grant 40334-AC6.

Appendix A. Supplementary data

Supplementary data associated with this article can be found, in the online version, at doi:10.1016/j.ijms.2007.06.016.

References

[1] J.D. Phillipson, M.H. Zenk, in: N. Neuss (Ed.), Indole and Related Alkaloids, Academic Press Inc., New York, 1980, p. 295.
[2] M.L. Hopp, M. Matsumoto, B. Wendell, C. Lee, R. Oyasu, Cancer Res. 36 (1976) 234.
[3] K. Heonicke, T.J. Simat, H. Steinhart, H.J. Köhler, A. Schwab, J. Agric. Food Chem. 49 (2001) 5494.
[4] K. Hoenicke, O. Borchert, K. Grüning, T.J. Simat, J. Agric. Food. Chem. 50 (2002) 4303.
[5] A.W. Woodward, B. Bartel, Ann. Bot. 95 (2005) 707.
[6] H. Matter, E. Defossa, U. Heinelt, P.M. Blohm, D. Schneider, A. Müller, S. Herok, H. Schreuder, A. Liesum, V. Brachvogel, P. Lönze, A. Walser, F. Al-Obeidi, P. Wildgoose, J. Med. Chem. 45 (2002) 2749.
[7] M. Himejima, I. Kubo, J. Agric. Food Chem. 41 (1993) 1776.
[8] E.B. Skibo, C. Xing, R.T. Dorr, J. Med. Chem. 44 (2001) 3545.
[9] R.E. Staub, C. Feng, B. Onisko, G.S. Bailey, G.L. Firestone, L.F. Bjeldanes, Chem. Res. Toxicol. 15 (2002) 101.
[10] M. Sechi, M. Derudas, R. Dallocchio, A. Dessi, A. Bacchi, L. Sannia, F. Carta, M. Palomba, O. Ragab, C. Chan, R. Shoemaker, S. Sei, R. Dayam, N. Neamati, J. Med. Chem. 47 (2004) 5298.
[11] K.R.F. Somers, E.S. Kryachko, A. Ceulemans, Chem. Phys. 301 (2004) 61.
[12] A.P. Demchenko, Ultraviolet Spectroscopy of Proteins, Springer, Berlin, 1986.
[13] S.V. Konev, Fluorescence and Phosphorescence of Proteins and Nucleic Acids, Plenum Press, New York, 1967.
[14] V. Ryzhov, R.C. Dunbar, J. Am. Chem. Soc. 121 (1999) 2259.

[15] C. Ruan, Z. Yang, N. Hallowita, M.T. Rodgers, J. Phys. Chem. A 109 (2005) 11539.
[16] M.T. Rodgers, P.B. Armentrout, Int. J. Mass Spectrom. 185–187 (1999) 359.
[17] R. Amunugama, M.T. Rodgers, Int. J. Mass Spectrom. 195/196 (2000) 439.
[18] M.T. Rodgers, J.R. Stanley, R. Amunugama, J. Am. Chem. Soc. 122 (2000) 10969.
[19] M.T. Rodgers, J. Phys. Chem. A 105 (2001) 2374.
[20] M.T. Rodgers, J. Phys. Chem. A 105 (2001) 8145.
[21] R. Amunugama, M.T. Rodgers, J. Phys. Chem. A 105 (2001) 9883.
[22] H. Huang, M.T. Rodgers, J. Phys. Chem. A 106 (2002) 4277.
[23] R. Amunugama, M.T. Rodgers, J. Phys. Chem. A 106 (2002) 5529.
[24] R. Amunugama, M.T. Rodgers, J. Phys. Chem. A 106 (2002) 9092.
[25] R. Amunugama, M.T. Rodgers, Int. J. Mass Spectrom. 227 (2003) 339.
[26] R. Amunugama, M.T. Rodgers, J. Phys. Chem. A 106 (2002) 9718.
[27] R. Amunugama, M.T. Rodgers, Int. J. Mass Spectrom. 222 (2003) 431.
[28] R. Amunugama, M.T. Rodgers, Int. J. Mass Spectrom. 227 (2003) 1.
[29] M.T. Rodgers, P.B. Armentrout, J. Am. Chem. Soc. 122 (2000) 8548.
[30] M.T. Rodgers, P.B. Armentrout, J. Am. Chem. Soc. 124 (2002) 2678.
[31] Z. Yang, M.T. Rodgers, J. Am. Chem. Soc. 126 (2004) 16217.
[32] Z. Yang, M.T. Rodgers, Int. J. Mass Spectrom. 241 (2005) 225.
[33] Z. Yang, M.T. Rodgers, J. Phys. Chem. A 110 (2006) 1455.
[34] N.S. Rannulu, R. Amunugama, Z. Yang, M.T. Rodgers, J. Phys. Chem. A 108 (2004) 6385.
[35] N.S. Rannulu, M.T. Rodgers, Phys. Chem. Chem. Phys. 7 (2005) 1014.
[36] C. Ruan, M.T. Rodgers, J. Am. Chem. Soc. 126 (2004) 14600.
[37] A.B. Valina, R. Amunugama, H. Huang, M.T. Rodgers, J. Phys. Chem. A 105 (2001) 11057.
[38] G. Vitale, A.B. Valina, H. Huang, R. Amunugama, M.T. Rodgers, J. Phys. Chem. A 105 (2001) 11351.
[39] M.T. Rodgers, P.B. Armentrout, J. Phys. Chem. A 101 (1997) 1238.
[40] M.T. Rodgers, P.B. Armentrout, J. Chem. Phys. 109 (1998) 1787.
[41] Y. Chu, Z. Yang, M.T. Rodgers, J. Am. Mass Spectrom. 13 (2002) 453.
[42] M.T. Rodgers, K.M. Ervin, P.B. Armentrout, J. Chem. Phys. 106 (1997) 4499.
[43] F. Muntean, L. Heumann, P.B. Armentrout, J. Chem. Phys. 116 (2002) 5593.
[44] F. Muntean, P.B. Armentrout, J. Phys. Chem. B 106 (2002) 8117.
[45] E. Teloy, D. Gerlich, Chem. Phys. 4 (1974) 417.
[46] D. Gerlich, Adv. Chem. Phys. 82 (1992) 1.
[47] K.M. Ervin, P.B. Armentrout, J. Chem. Phys. 83 (1985) 166.
[48] N.F. Dalleska, K. Honma, L.S. Sunderlin, P.B. Armentrout, J. Am. Chem. Soc. 116 (1994) 3519.
[49] M.J. Frisch, G.W. Trucks, H.B. Schlegel, G.E. Scuseria, M.A. Robb, J.R. Cheeseman, V.G. Zakrzewski, J.A. Montgomery Jr., R.E. Stratmann, J.C. Burant, S. Dapprich, J.M. Millam, A.D. Daniels, K.N. Kudin, M.C. Strain, O. Farkas, J. Tomasi, V. Barone, M. Cossi, R. Cammi, B. Mennucci, C. Pomelli, C. Adamo, S. Clifford, J. Ochterski, G.A. Petersson, P.Y. Ayala, Q. Cui, K. Morokuma, D.K. Malick, A.D. Rabuck, K. Raghavachari, J.B. Foresman, J. Cioslowski, J.V. Ortiz, B.B. Stefanov, G. Liu, A. Liashenko, P. Piskorz, I. Komaromi, R. Gomperts, R.L. Martin, D.J. Fox, T. Keith, M.A. Al-Laham, C.Y. Peng, A. Nanayakkara, C. Gonzalez, M. Challacombe, P.M.W. Gill, B. Johnson, W. Chen, M.W. Wong, J.L. Andres, C. Gonzales, M. Head-Gordon, E.S. Replogle, J.A. Pople, Gaussian 98, Revision A.9, Gaussian, Inc., Pittsburgh, PA, 1998.
[50] C. Adamo, V.J. Barone, J. Chem. Phys. 108 (1998) 664.
[51] Listing of precomputed vibrational scaling factors (XIII.C.1), NIST Computational Chemistry Comparison and Benchmark Database, Released May 11, 2005, NIST Standard Reference Database 101 (http://srdata.nist.gov/cccbdb/).
[52] S.F. Boys, R. Bernardi, Mol. Phys. 19 (1979) 553.
[53] F.B. van Duijneveldt, J.G.C.M. van Duijneveldt-van de Rijdt, J.H. van Lenthe, Chem. Rev. 94 (1994) 1873.
[54] F. Muntean, P.B. Armentrout, J. Chem. Phys. 115 (2001) 1213.
[55] T.S. Beyer, D.F. Swinehart, Commun. Assoc. Comput. Mach. 58 (1973) 2438.
[56] F.A. Khan, D.E. Clemmer, P.B. Armentrout, J. Phys. Chem. 113 (1993) 7978.
[57] G. Sindona, N. Uccella, Int. J. Mass Spectrom. Ion Process. 63 (1985) 49.
[58] E.P. Hunter, S.G. Lias, J. Phys. Chem. Ref. Data 27 (1998) 413.
[59] W.A. Hinmann, E.B. Whipple, J. Am. Chem. Soc. 84 (1962) 2534.